
Article:
Weese, J., Lungu, A., Peters, J. et al. (3 more authors) (2017) CDF- and Bernoulli-based pressure drop estimates: a comparison using patient anatomies from heart and aortic valve segmentation of CT images. Medical Physics, 44 (6). pp. 2281-2292. ISSN 0094-2405

https://doi.org/10.1002/mp.12203

CFD- and Bernoulli-based pressure drop estimates: A comparison using patient anatomies from heart and aortic valve segmentation of CT images

J. Weese,[1] A. Lungu,[2] J. Peters,[1] F.M. Weber,[1] I. Waechter-Stehle,[1] and D.R. Hose[2]

[1)] *Philips Research Laboratories, Röntgenstrasse 24-26, D-22335 Hamburg, Germany*

[2)] *Medical Physics Group, The University of Sheffield, Medical School, Beech Hill Road, Sheffield, S10 2RX, United Kingdom*

(Dated: 8 February 2017)

Purpose: An aortic valve stenosis is an abnormal narrowing of the aortic valve (AV). It impedes blood flow and is often quantified by the geometric orifice area of the AV (AVA) and the pressure drop (PD). Using the Bernoulli equation, a relation between the PD and the effective orifice area (EOA) represented by the area of the vena contracta (VC) downstream of the AV can be derived. We investigate the relation between the AVA and the EOA using patient anatomies derived from cardiac computed tomography (CT) angiography images and computational fluid dynamic (CFD) simulations.

Methods: We developed a shape-constrained deformable model for segmenting the AV, the ascending aorta (AA) and the left ventricle (LV) in cardiac CT images. In particular, we designed a structured AV mesh model, trained the model on CT scans, and integrated it with an available model for heart segmentation. The planimetric AVA was determined from the cross-sectional slice with minimum AV opening area. In addition, the AVA was determined as the non-obstructed area along the AV axis by projecting the AV leaflet rims on a plane perpendicular to the AV axis. The flow rate was derived from the LV volume change. Steady-state CFD simulations were performed on the patient anatomies resulting from segmentation.

Results: Heart and valve segmentation was used to retrospectively analyze 22 cardiac CT angiography image sequences of patients with non-calcified and (partially) severely calcified tricuspid AVs. Resulting AVAs were in the range of $1 - 4.5\text{cm}^2$ and ejection fractions (EFs) between $20 - 75\%$. AVA values computed by projection were smaller than those computed by planimetry, and both were strongly correlated ($R^2 = 0.995$). EOA values computed via the Bernoulli equation from CFD-based PD results were strongly correlated to both AVA values ($R^2 = 0.97$). EOA values were $\sim 10\%$ smaller than planimetric AVA values. For EOA values $< 2.0\text{cm}^2$, the EOA was up to $\sim 15\%$ larger than the projected AVA.

Conclusions: The presented segmentation algorithm allowed to construct detailed AV models for 22 patient cases. Because of the crown-like 3D structure of the AV, the planimetric AVA is larger than the projected AVA formed by the free edges of the AV leaflets. The AVA formed by the free edges of the AV leaflets was smaller than the EOA for EOA values $< 2.0\text{cm}^2$. This contradiction with respect to previous studies that reported the EOA to be always smaller or equal to the geometric AVA

is explained by the more detailed AV models used within this study.

I. INTRODUCTION

Aortic valve stenosis[1] is an abnormal narrowing of the aortic valve (AV) that impedes blood flow. In patients with age over 65, AV stenosis is most often caused by calcification that prevents proper valve opening and closing. The pressure drop (PD) that is usually assessed by Doppler-echocardiography[2] describes to what extent improper valve opening impedes blood flow. Another measure of AV stenosis severity is the geometric aortic valve opening area (AVA), which is usually determined by planimetry in echocardiography[2] or cardiac computed tomography (CT) angiography[3] images. CT images provide the highest-resolution anatomic data of the AV in calcific aortic stenosis and allow to assess the amount of calcification, but have a limited temporal resolution and do not provide hemodynamic data such as the PD[1].

Often, the effective orifice area (EOA) represented by the area of the vena contracta (VC) downstream of the AV is used to characterize the valve orifice and not the AVA. The EOA can, for instance, be computed from the PD, blood flow rate and the cross-sectional area of the left ventricular outflow tract (LVOT) using the Bernoulli equation. Both quantities, EOA and AVA are different, but understanding the relation between EOA and AVA is important for a consistent interpretation of anatomical and flow-dependent indices of AV stenosis severity. Therefore, the relation between AVA and EOA has been investigated, for instance, in in-vitro studies that use AV models produced by stereolithography with anatomies derived from echocardiography[4]. In addition, simple geometric models representing the AV have been investigated theoretically and fluid mechanics theory shows for these models that the EOA is always smaller (up to 40%) or equal (e.g. for a funnel-shaped aortic stenosis) to the geometric AVA[5].

We developed a simulation pipeline to investigate the relation between geometric AVA and EOA using patient anatomies derived from cardiac CT angiography images (Fig. 1). Its key element is a method for segmenting the heart and the AV in cardiac CT angiography image sequences. The segmentation result defines the simulation domain for a steady-state simulation of the blood flow through the AV with a flow rate derived from the left ventricular (LV) volume change. EOA values are calculated via the Bernoulli equation from PD results and compared with geometric AVA measurements.

Compared to Ref. 4, CT images have been used that have a much higher spatial resolution

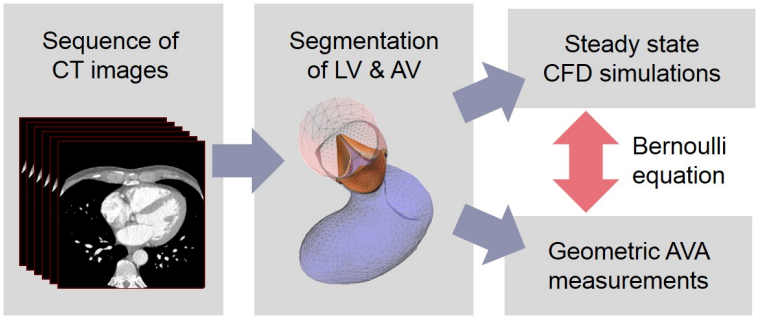

FIG. 1. Illustration of the in-silico approach for comparing geometric AVA measurements and EOA values computed via the Bernoulli equation from CFD-based PD estimates.

than echocardiography images and enable the AV models to be derived more accurately. For accurately segmenting the heart and the aortic valve, several methods have been developed for CT images and 3D ultrasound (US) sequences that use generic models of the AV and other heart structures that are adapted to patient images[6–10]. Compared to previous work, we focus on the robust segmentation of the AV in the presence of calcifications. We built our work on the SCDM framework[11,12] and extend the segmentation for transcatheter AV intervention planning[7,13] to opened and closed valve states of patients with tricuspid and possibly calcified AVs. While previous work related to blood flow simulations in the AV focused on comprehensive FSI simulations[14–18] that have mostly been applied to very few patient cases, we use simple steady-state blood flow simulations, apply them to AV geometries of 22 patient cases and show that the use of detailed AV anatomies leads to new insights when comparing EOA and geometric AVA.

After briefly introducing the SCDM segmentation framework in Sec. II A, we provide a detailed description of the design of our structured AV mesh model (Sec. II B). The AV mesh model was trained using cardiac CT angiography images and integrated into an available model for heart segmentation (Sec. II C). The Bernoulli equation and the computation of geometric quantities like AVA on the basis of a segmentation are described in Sec. II D. The CFD simulations are described in Sec. II E. Results for heart and AV segmentation are included in Sec. III A. The processing pipeline was applied to 22 cardiac CT angiography image sequences, and EOA computed via the Bernoulli equation from CFD-based PD estimates were compared with AVA measurements. The results are presented in Sec. III B. Sec. IV includes a discussion of the results. Our conclusions are summarized in Sec. V.

The paper extends a conference contribution[19], describes the methods in more detail, and includes additional results.

II. METHOD

A. Shape-constrained deformable models

Within the SCDM framework[11,12] a mesh model of the target anatomy with V vertices $\boldsymbol{m}_1, \ldots, \boldsymbol{m}_V$ and T triangles is adapted to an image. First, the anatomical structure is detected using the Generalized Hough Transformation (GHT). Afterwards, parametric model adaptation is performed. For that purpose, the model is transformed according to $\mathcal{T}(\boldsymbol{q})[\boldsymbol{m}_k]$ with $\boldsymbol{q}$ describing the transformation parameters. Boundary points $\boldsymbol{x}_i^{\mathrm{t}}$ are detected along profiles parallel to the triangle normals using individually trained boundary detectors F_i for each triangle i, and the transformation parameters $\boldsymbol{q}$ are updated by minimizing the external energy[11]

$$E_{\mathrm{ext}} = \sum_{i=1}^{T} \tilde{w}_i \left(\frac{\boldsymbol{\nabla} I(\boldsymbol{x}_i^{\mathrm{t}})}{\parallel \boldsymbol{\nabla} I(\boldsymbol{x}_i^{\mathrm{t}}) \parallel} (\boldsymbol{x}_i^{\mathrm{t}} - \boldsymbol{c}_i(\boldsymbol{q})) \right)^2, \tag{1}$$

where I denotes the image. The weights $\tilde{w}_i$ characterize confidence in a boundary. The triangle centers $\boldsymbol{c}_i(\boldsymbol{q})$ are calculated from the transformed vertices $\mathcal{T}(\boldsymbol{q})[\boldsymbol{m}_j]$ forming the triangle i. Boundary detection and refinement of the parameters $\boldsymbol{q}$ are iterated several times to complete a parametric adaptation step.

Parametric adaptation may be done in several stages. Initially, a similarity transformation $\mathcal{T}_{\mathrm{sim}}$ may be used. Later, adaptation may be refined using a multi-linear transformation[11]

$$\mathcal{T}_{\mathrm{multi-linear}}(\boldsymbol{q})[\boldsymbol{m}_i] = \sum_{k=1}^{K} w_{i,k} \cdot \mathcal{T}_k(\boldsymbol{q}_k)[\boldsymbol{m}_i], \tag{2}$$

with weights $w_{i,k}$ defining a fuzzy subdivision of the model into K parts. In a final stage, adaptation is performed by iterating boundary detection and mesh deformation. Mesh deformation optimizes the energy $E = E_{\mathrm{ext}} + \alpha E_{\mathrm{int}}$ composed of the external energy of eq. (1) and the internal energy[11]

$$E_{\mathrm{int}} = \sum_{i=1}^{V} \sum_{j \in \mathcal{N}_i} \sum_{k=1}^{K} w_{i,k} \left(\boldsymbol{x}_i - \boldsymbol{x}_j - \mathcal{T}_k(\boldsymbol{q}_k)[\boldsymbol{m}_i - \boldsymbol{m}_j] \right)^2 \tag{3}$$

in dependence of the vertex coordinates $\boldsymbol{x}_i$ and the transformation parameters $\boldsymbol{q}_k$. $\mathcal{N}_i$ is the set of neighbors of vertex i. The weight α controls to what extent deviations between adapted mesh and reference shape are penalized.

B. Aortic valve model

The anatomy of the AV has been described in several publications[20] and related mesh models have been designed for the purpose of segmentation[6,7,9] and biomechanical modeling[21]. In the following we describe the generation of a high quality AV mesh model. Compared to the model of Ref. 6, the model is integrated with a full heart model and facilitates setting up the domain for CFD simulations. Compared to the model of Refs. 7 and 9 that has been generated from binary masks, our AV mesh is structured and better represents details such as the rim of the leaflets. The model of Ref. 21 provides also high mesh quality, but was not integrated in an efficient segmentation framework.

The starting point of the AV mesh model is a double layered "wedge" (Fig. 2a) representing a single AV leaflet. Three wedges represent the AV leaflets in the closed state. The AV leaflets have been complemented by a tubular structure in direction of the ascending aorta (AA) and one in direction of the LV outflow tract (LVOT) (Fig. 2b).

The AV mesh model includes additional information that facilitates segmentation. In particular, each "wedge" includes connections between the upper and the lower layer (Fig. 2c). These connections add further terms to the internal energy of eq. (3) by including corresponding vertices of the upper and lower layer of a "wedge" in the set $\mathcal{N}_i$. The connections help to prevent intersections between both layers during segmentation. In addition, the AV mesh model contains a set C_{coapt} of connections between the vertices at the coaptation edges of the valve leaflets. For a closed valve, we add the term

$$E_{\text{close}} = \sum_{(i,j)\in C_{\text{coapt}}} (\boldsymbol{x}_i - \boldsymbol{x}_j)^2 \tag{4}$$

to the energy E that minimizes the distance between vertices at the coaptation line, ensures that the AV is closed, and prevents that different AV leaflets overlap.

The mesh model of Fig. 2 does not show the typical shape of the AV and the surrounding structures. To generate this shape and also provide annotated image data for boundary detection training (see Sec. II C), 147 anonymized cardiac CT angiography scans from 57

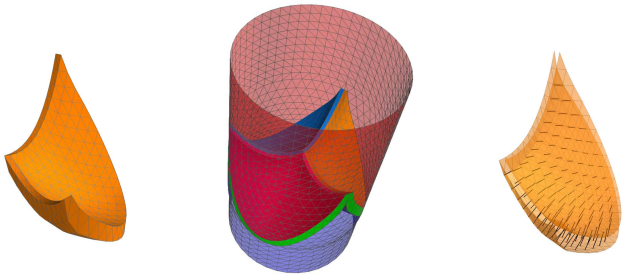

(a) (b) (c)

FIG. 2. Illustration of the design of the aortic valve mesh (a–b). The connections between the layers building the valve leaflets are shown in (c).

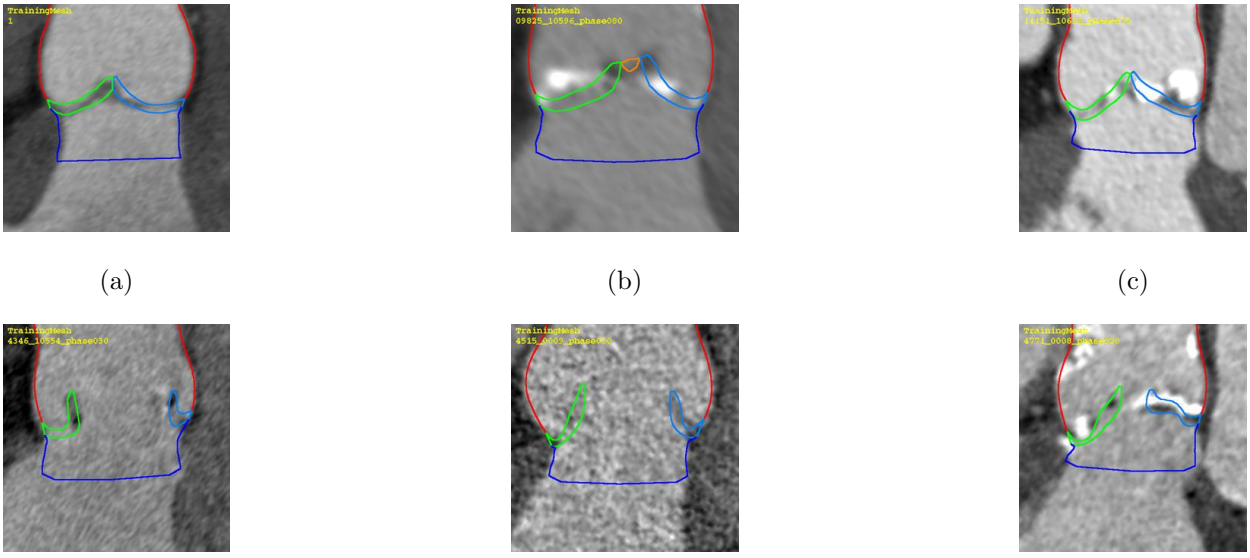

(a) (b) (c)

(d) (e) (f)

FIG. 3. Cross-sections of CT images with closed (a–c) and open (d–f) aortic valve. The colored contours represent the reference segmentation.

patients were retrospectively analyzed. The mesh model was semi-automatically adapted to the 147 images using the previously described bootstrap approach[11]. The CT images had an in-plane resolution of 0.30×0.30 - $0.78\times0.78\,\mathrm{mm}^2$ and a slice thickness of 0.33 - 1.00 mm. The data covered closed (diastasis; $70-80\%$ of the electrocardiographic R-R interval) and open (mid-systole; $20-30\%$ of the electrocardiographic R-R interval) valve states from subjects with healthy (without calcification) or stenosed (partially with severe calcifications) valves. Fig. 3 shows some examples.

To guide segmentation of the AV in different opening states, we calculated a mean mesh

from a set of closed valves with vertices $\bar{\boldsymbol{m}}_i^{cl}$ and another mean mesh with vertices $\bar{\boldsymbol{m}}_i^{op}$ representing healthy valves in the open state. Similar to Ref. 9, both mean meshes were combined into a point distribution model (PDM):

$$\boldsymbol{m}_i(p) = \frac{1}{2}\left(\bar{\boldsymbol{m}}_i^{cl} + \bar{\boldsymbol{m}}_i^{op}\right) + \frac{p}{2}\left(\bar{\boldsymbol{m}}_i^{cl} - \bar{\boldsymbol{m}}_i^{op}\right). \tag{5}$$

Opening and closing of the valve can thus be described by the parameter p. During SCDM adaptation, deformation modeling by multi-linear transformations is combined with the PDM by inserting eq. (5) into the internal energy of eq. (3) and the parameter p is optimized in addition to the vertex positions $\boldsymbol{x}_i$ and the transformation parameters $\boldsymbol{q}_k$. It should be emphasized that the opening state of the segmentation is not simply a linear interpolation of open and closed valve states, because the internal energy of eq. (3) allows the SCDM-based segmentation result to deviate from the shape model.

C. Model training and adaptation

The boundary detection functions F_i use gradient information in direction of the mesh normal $\boldsymbol{n}_i$ to detect boundaries. Different features $Q_j(\boldsymbol{x})$ like average gray-values on one or the other side of the considered boundary are computed, and only boundaries with feature values inside triangle-specific acceptance intervals are retained.

Specific boundary detection functions F_i have been used to enable reliable segmentation of the AV leaflets that can be either clearly visible, noisy, or severely distorted by calcification. In particular, gray values are evaluated on a hexagonal grid (19 sampling points; 1 mm distance) in planes parallel to the triangle. The image gradient $\boldsymbol{\nabla} I(\boldsymbol{x})$ is approximated by the scaled difference of the average gray value on two planes on both sides of the considered boundary point. The gray values on either side of the boundary averaged over 1, 2 or 4 points along the triangle normal are used as clipping criteria $Q_j(\boldsymbol{x})$. Additional clipping criteria are (i) the difference of the average gray value on both sides of the boundary, (ii) the variance of several profile points, (iii) the variance of the gray values within a hexagonal grid, and (iv) gradient values on either side of the boundary. All quantities were evaluated at the reference boundaries of the training images, k-means clustering was applied and acceptance intervals were derived. By using different clustering parameters and by combining different clipping criteria, two sets of boundary detector candidates were generated for coarse and for fine boundary detection.

Boundary detectors were assigned to a triangle using penalized "Simulated Search"[22,23]. In this approach a triangle is displaced, boundary detection is performed using a specific detector and the Euclidean boundary detection error is recorded. It is also recorded whether a boundary is detected in an undesired region, in particular, if a boundary for the AV leaflet triangles on the side of the aortic bulbus was detected on the side of the LVOT and vice versa. Simulation of boundary detection is done for multiple displacements and all training images resulting in an average detection error $d(F,i)$ and a fraction $p(F,i)$ of undesired detections. After simulation, the detector F is selected for triangle i that minimizes a weighted sum of the detection error $d(F,i)$ and the fraction $p(F,i)$ of undesired detections. For coarse boundary detection, profiles of length $\pm 10\,\mathrm{mm}$ with $1\,\mathrm{mm}$ point spacing, 263513 boundary detector candidates, 147 displacements, and a weighting of $d(F,i) + 1.765\,p(F,i)$ were used. For fine boundary detection with $\pm 2\,\mathrm{mm}$ profile length and $0.5\,\mathrm{mm}$ point spacing, training used 504025 candidates, 63 displacements and undesired detections were not penalized.

The AV model was integrated into a heart model including the ascending aorta[12]. We used the training images of Ref. 23 to train the boundary detectors of the aortic bulbus. In addition, we mapped the boundary detection functions of Ref. 23 onto the LV epi- and endocardium to increase segmentation accuracy. Model adaptation follows the processing chain of Ref. 12. The initial adaptation steps are performed with a half open AV ($p = 0$). During final deformable adaptation, the AV leaflets are adapted. Within an additional refinement step, AV and LV segmentation are improved using fine boundary detection (see above text for the AV and Ref. 23 for the LV). If a closed valve is detected, the energy term of eq. (4) is added during the final iteration.

D. Bernoulli equation, EOA and AVA

Fig. 4 illustrates blood flow through the AV[5]. Blood passes the LVOT with cross-sectional area A_{LVOT} and flow rate Q, flows into the AV with opening area A_{AV} and builds the VC, which corresponds to the location where the cross-sectional area of the jet is minimal. The corresponding cross-sectional area is called EOA and denoted by A_{EOA}. Afterwards, the blood passes the aortic bulbus and enters the ascending aorta (AA). The (static) pressure p_{LVOT} drops while passing the AV to a minimum of p_{VC} and increases again in the AA.

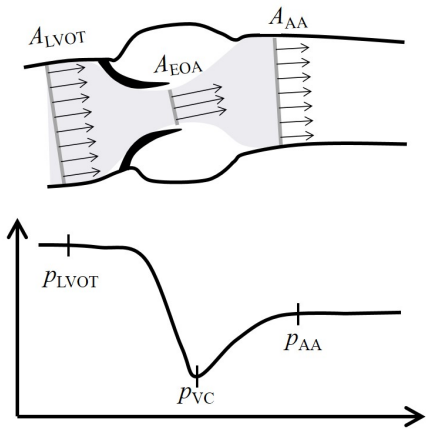

FIG. 4. Sketch illustrating blood flow through the AV and the (static) blood pressure from LVOT to the AA.

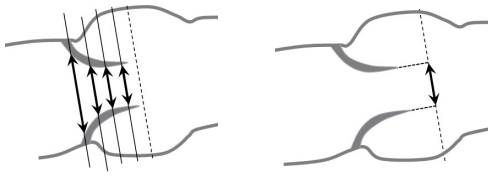

(a) (b)

FIG. 5. Sketch illustrating AVA measurement by planimetry (a) and by projection (b).

Using the Bernoulli equation, the EOA can be related to the PD $\Delta p = p_{\mathrm{LVOT}} - p_{\mathrm{VC}}$:

$$\Delta p = \frac{1}{2}\rho Q^2 \left(\left(\frac{1}{A_{\mathrm{EOA}}} \right)^2 - \left(\frac{1}{A_{\mathrm{LVOT}}} \right)^2 \right). \tag{6}$$

using the blood density ρ and the flow rate Q[5]. The flow rate

$$Q(t) = \frac{\partial}{\partial \phi} V_{\mathrm{LV}}(\phi)\ \frac{d\phi}{dt}. \tag{7}$$

can be computed from the change of the LV volume $V_{LV}(\Phi)$ over the heart phase Φ and the heart beats per minute $\frac{d\phi}{dt}$.

While the EOA can be computed via eq.(6) from the PD resulting from blood flow simulations, the other quantities can be inferred from the segmentation result. The LV volume can easily be computed using the segmentation results for the endocardial LV border. The cross-sectional area A_{LVOT} can be obtained by cutting the segmentation result for the LVOT perpendicular to its axis[7].

Computation of the geometric AVA formed by the free edges of the AV leaflets[1] is more complicated. In clinical studies, planimetry is used[3], and an analogous approach was imple-

mented using the segmentation result. Starting at the AV annulus plane, cross-sections were generated perpendicular to the AV axis and the orifice area was measured. The plane was shifted towards the AA until the valve leaflets stopped to build a contiguous opening, and the minimum orifice area was selected as AVA measurement A_{AVplan}. This approach may, however, result in a larger apparent orifice area proximal to the cusp tips. For that reason, an approach was implemented that measures the geometric area formed by the free edges of the AV leaflets. In particular, the AV leaflet rims were projected on a plane perpendicular to the AV axis to approximate the area not obstructed by the AV in 3D. The associated AVA measurement is denoted by A_{AVproj}. Fig. 5 illustrates both approaches. While the planimetric and the projected AVA are the same for the example in Fig. 5, they differ for the complex crown-like 3D structure of the AV.

E. CFD simulations

To generate the mesh for the CFD simulations, the axis of the LVOT and of the AA were determined. The segmentation mesh was cut perpendicular to each axis to obtain a model of the LVOT, the open AV, the aortic sinuses and an initial part of the AA. Inlet and outlet tubes were added by extending the shape of the inlet and outlet cross-section along respective axis for a length given by three times the radius. The resolution of the surface mesh was increased and the surface was smoothed to generate a mesh with sufficient resolution. Volumetric meshing was performed using ICEM v14.0. Mesh sensitivity tests (i.e. CFD simulations with increasing mesh resolution) were carried out for each individual case. In particular, a root mean squared (RMS) residual of pressure and momentum smaller than 10^{-5} was chosen as convergence criterium. Each resulting model consisted of approximately 2.5 - 3.5 million elements, typically one third of which were pentahedral elements inflated from the wall and two thirds tetrahedral elements in the core of the flow domain.

For the steady-state CFD simulations, the blood was assumed to be an incompressible Newtonian fluid with density of 1056 $\mathrm{kg/m^3}$ and viscosity of 0.004 Pa s. The vessel walls were considered to be rigid and the fluid velocity at the walls to be zero (no-slip). The volumetric flow rate at the inlet was determined from the LV volume change and identical values were used for the Bernoulli-based analysis. For consistency with clinical expectation, a pressure of 16000 Pa (120 mmHg) has been applied at the distal boundary to represent the pressure

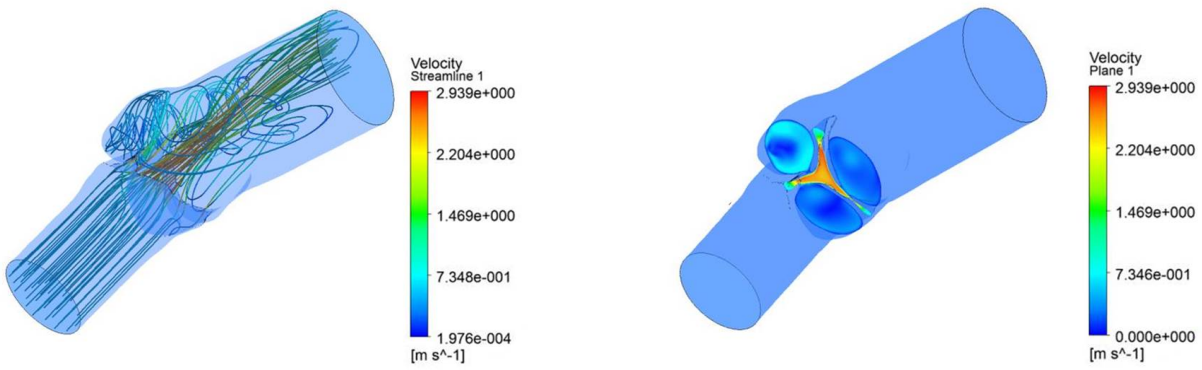

FIG. 6. Example of the model geometry used for CFD simulations. The model is displayed together with the velocity streamlines passing through the AV and the velocity distribution on an AV plane.

in the AA at peak systole. This boundary condition does only influence absolute pressure values, but has no influence on pressure differences derived from the CFD simulations.

The governing Navier Stokes and continuity equations were solved using an element-based finite volume method with co-located grid (non staggered grid) and a shear stress transport (SST) turbulence model through ANSYS-CFX v14.0. An exemplary simulation result is shown in Fig. 6. The Reynolds number in the throat of the valve, based on equivalent diameter, varied between 3400 and 11100, justifying the use of a turbulence model. Furthermore, the SST model was the most commonly employed model by the 28 investigators who submitted results to the FDA Critical Path initiative for a nozzle system at similar Reynolds numbers[24]. Results for the FDA initiative using the particular transitional SST turbulence model employed in our simulations show good correlation with the published experimental data[25]. In addition, a detailed comparison of laminar versus turbulent models in the context of a thoracic aortic aneurysm[26] demonstrated that the transitional SST model gave a better correlation with measured flow fields than the laminar one.

III. RESULTS

A. Left ventricle and aortic valve segmentation

Heart and AV segmentation was applied to the 147 training images and automatic segmentation did work for 143 of these cases. Visual inspection of the segmentation results showed that the connections between valve leaflet surfaces and boundary detection train-

ing with penalties enabled good segmentations to be obtained. Implausible adaptations to the wrong surface could almost completely be avoided. Due to the use of a shape model, segmentations tend to be smoother than a voxelwise manual annotation. Fig. 7 and Fig. 8 show models and segmentation results for different heart phases of 2 patient cases that have not been used for model training.

Information about the segmentation accuracy can be obtained from previous publications and the data used for training. A mean constrained symmetric surface-to-surface (CSStS) error that restricts search of the closest mesh point to a geodesic neighborhood of 10 mm radius around the corresponding mesh point of 0.6–0.8 mm has been reported for the LV and the aorta using test datasets independent of the training data sets[12]. For improved LV segmentation a mean CSStS error of 0.7–0.8 mm has been reported using 3-fold cross-validation on 67 datasets[23]. For the AV leaflets, a geodesic radius of 5 mm was used to account for the smaller size of these structures and a mean CSStS error of 0.47 mm is obtained on the 143 cases of the training data. This error is in the order of the image resolution and of the same magnitude as the constrained mesh-to-mesh distance of 0.6 mm between two reference segmentations generated for one data set. Because of the complex model building process, cross-validation was too complex and formal evaluation of the segmentation accuracy would need to be done on independent data.

The comparison between geometric AVA and EOA just uses the mesh geometries and is not influenced by inaccuracies of the segmentation algorithm as long as realistic patient anatomies are obtained. For that reason, visual inspection of the segmentation results is sufficient in this context and a comprehensive evaluation of the segmentation accuracy was not performed.

B. Geometric AVA and EOA

For comparing EOA with geometric AVA, anonymized cardiac CT angiography datasets of 22 patients with non-calcified and (partially) severly calcified tricuspid AVs have been used and retrospectively analyzed. The datasets had a resolution of $0.31 - 0.68$ mm in-plane and a slice thickness of $0.34 - 0.70$ mm. For each case, reconstructions for $0\%, 10\%, \ldots, 90\%$ of the heart cycle were available. The mean heart rate of the datasets ranged between $51 - 98$ BPM.

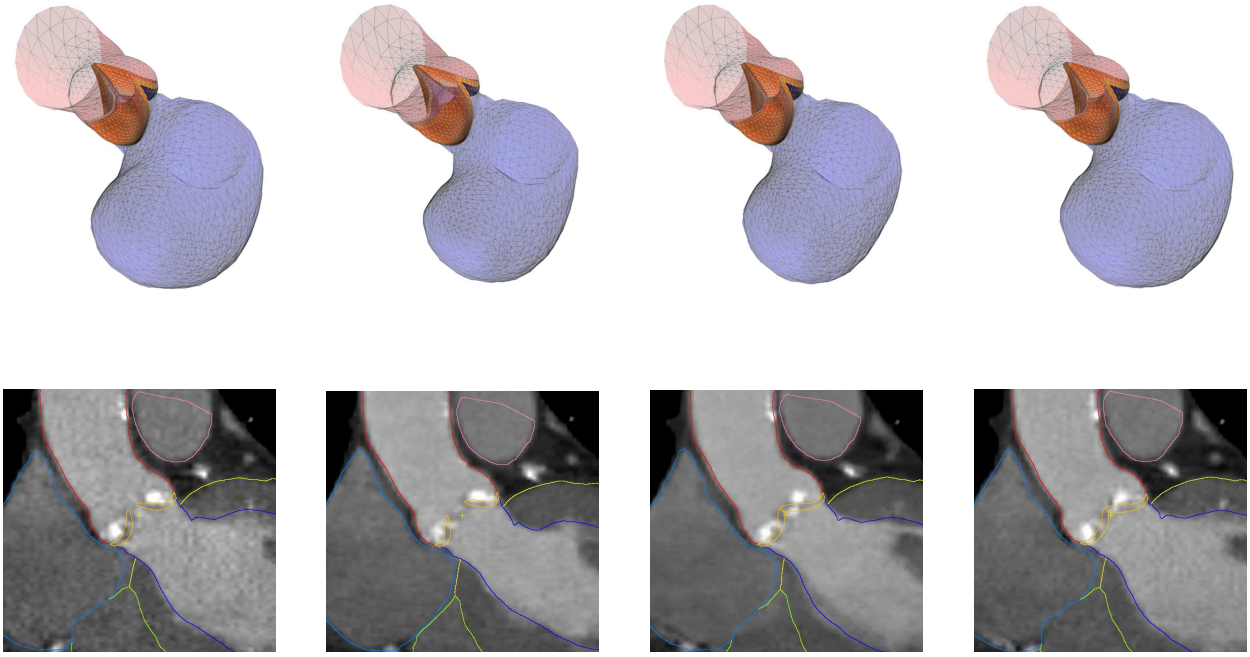

FIG. 7. Segmentation result of a patient showing little LV contraction while the AV is opening. The heart phase is given as percentage of the length of the R-R interval and 0% corresponds to late diastole / beginning of systole.

Automatic heart and valve segmentation was applied to the 22 image sequences and the results have been visually inspected. The subsequent analysis was based on the mesh models resulting from segmentation. In particular, LV volumes were computed. The AVA was determined by projection, because the planimetric AVA may not be zero if the AV is closed. Fig. 9 shows a plot of both quantities over the heart cycle for two cases. In both cases, the valve opens when the LV starts to contract and closes when the LV relaxes again. In the case of a non-stenosed AV (Fig. 9a), the valve opens properly resulting in an AVA of $3.34\,\mathrm{cm}^2$ for the open AV. In the case of an AV stenosis (Fig. 9b), an AVA of $0.88 - 0.95\,\mathrm{cm}^2$ is obtained.

CFD simulations were performed for the heart phase with maximum AVA using a volume flow Q estimated from LV volumes at the selected heart phase $\pm 10\%$ and the heart beats per minute (BPM). If this phase was ambiguous, the heart phase with larger LV contraction and volume flow Q was taken. In addition, the cross-sectional area at the LVOT and the AA were determined[7]. Eq. (6) was used to compute the EOA from the CFD-based PD results.

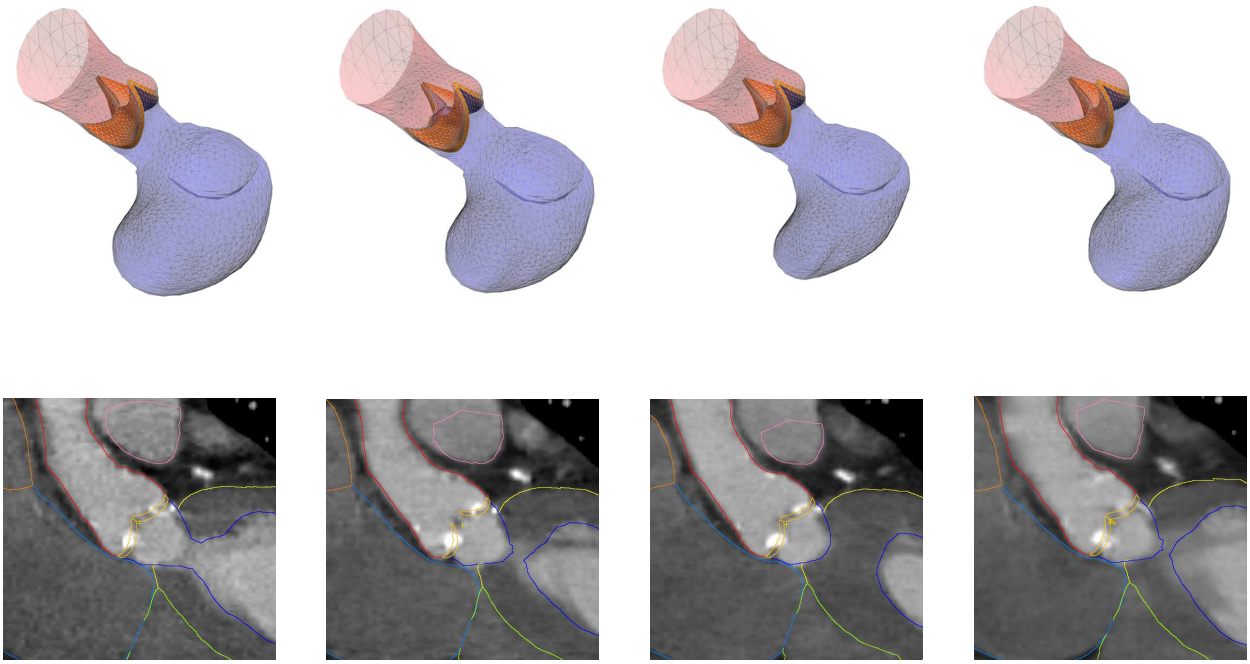

0% 20% 30% 60%

FIG. 8. Segmentation result of a patient having a AV stenosis and showing considerable LV contraction. The heart phase is given as percentage of the length of the R-R interval and 0% corresponds to late diastole / beginning of systole.

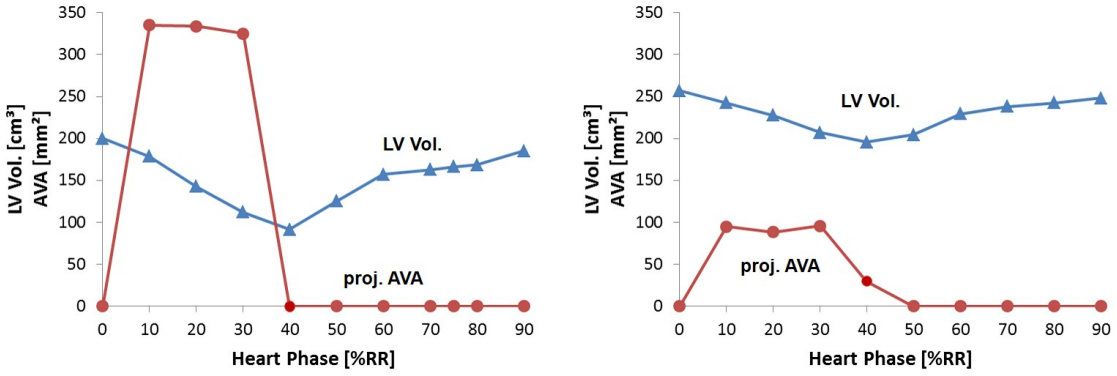

(a) (b)

FIG. 9. LV Volume and AVA computed by projection over the heart cycle for a case without (a; case 18) and with (b; case 9) AV stenosis. The heart phase is given by the percentage of the length of the electrocardiographic R-R interval and 0% corresponds to late diastole / beginning of systole.

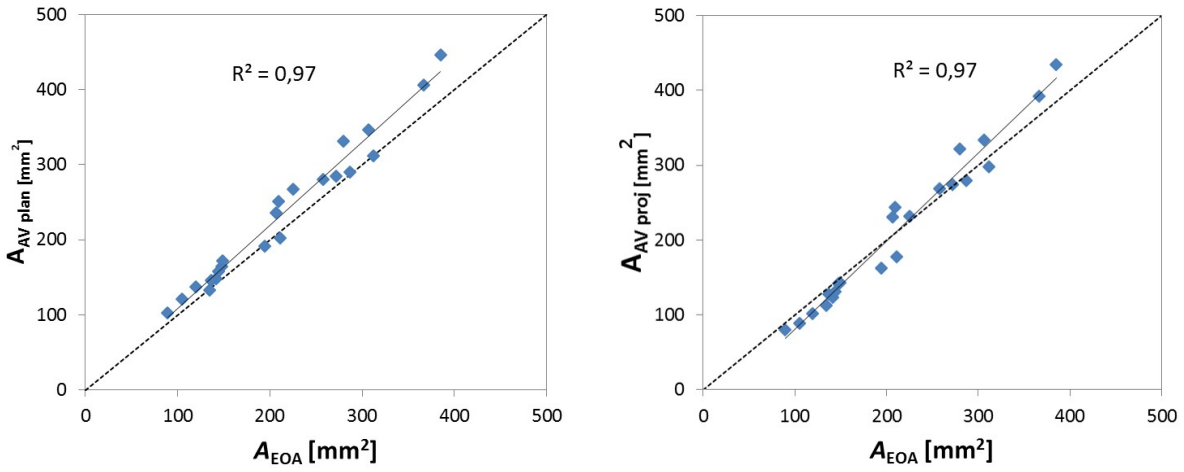

(a) (b)

FIG. 10. Plots of the CFD-based EOA measurements vs. geometric AVA computed by planimetry (a) and by projection (b). The coefficient of determination was computed according to $R^2 = \frac{(\sum (x_i - \bar{x})(y_i - \bar{y}))^2}{\sum (x_i - \bar{x})^2 \sum (y_i - \bar{y})^2}$.

All values are included in Table I.

AVA values determined by projection are smaller than those computed by planimetry, and both are strongly correlated ($R^2 = 0.995$). For small AVA of about $1\,\mathrm{cm}^2$ the difference can be up to $20 - 25\%$. Fig. 10 shows that AVA measurements and CFD-based EOA estimates are strongly correlated ($R^2 = 0.97$). EOA values were $\sim 10\%$ smaller than planimetric AVA values. For EOA values $< 2.0\mathrm{cm}^2$, the EOA was up to $\sim 15\%$ larger than the projected AVA.

C. Sensitivity Analysis

The results in Tab. I are influenced by segmentation inaccuracies and approximations. Ref. 7 suggests, for example, that segmentation inaccuracies lead to an RMS error of the LVOT diameter of $1 - 1.2\,\mathrm{mm}$. Fig. 7 and 8 illustrate that AV segmentation works in the presence of calcifications, but segmentation inaccuracies in the presence of strong calcifications might be present and difficult to detect, because of image artifacts. The calcifications themselves are not represented in the segmentation results and the corresponding mesh models, but are likely to influence the blood flow. In addition, results are affected by the limited

temporal resolution of the CT images, and the heart phase with the maximum opening of the AV might not have been captured. The limited temporal resolution can also lead to an underestimation of the flow rate Q that is estimated from the LV volume change. In addition, the computation of flow rates from LV volume change neglects possible mitral valve regurgitation. While these inaccuracies affect the measurements obtained for an individual patient, they do not limit the comparison between AVA and EOA. All quantities that are used in the comparison for a patient case such as the anatomical mesh for the CFD simulation, geometric measurements and flow rate Q are derived from the same segmentation result.

For the CFD simulations, mesh sensitivity tests (i.e. CFD simulations with increasing mesh resolution) were carried out for each individual case and a root mean squared (RMS) residual of pressure and momentum smaller than 10^{-5} was chosen as convergence criterium (see Sec. II E). Additional CFD simulations have been performed for two cases (12 and 15) with AV stenosis and large PD. In order to ensure that the results are independent of spatial discretisation, the Richardson's extrapolation method[27] was employed, based on three different mesh sizes (1.6, 2.6 and 3.5 million elements). The relative error between the inlet pressure returned by the model with the finest mesh used to generate the results in Table I and the inlet pressure returned by the Richardson prediction method was 0.11% (Case 12) and 0.03% (Case 15).

In addition, CFD simulations were performed for these two cases to provide an indication of the sensitivity of our simulations to the adopted flow model. First, simulations with a laminar flow assumption instead of the turbulence model were conducted. Second, transient flow simulations have been performed to analyze the inaccuracy resulting from the steady-state assumption. For these simulations, the flow rates estimated from the LV volume change over time were interpolated using gradient-continuous piecewise cubic splines, while keeping the valve anatomy fixed with the valve fully open. The time varying mass flow rate was prescribed for the inlet boundary. The outlet and wall boundary conditions were kept the same as for the steady-state simulations (constant pressure, rigid wall with no slip condition). The equations were solved over three cardiac cycles, using a second order backward Euler numerical scheme, with a time step of 0.01 s and zero blood flow velocity initial condition. The (peak) PD was computed at the maximum flow rate. The results are included in Table II.

Using the laminar flow model instead of the turbulence model, estimated PD increased by $1.5 - 2.2\,\mathrm{mmHg}$ or $6 - 10\%$. For the transient flow simulations, PD estimates increase by $\sim 1\,\mathrm{mmHg}$ or $\sim 4\%$. EOA decrease by up to $\sim 4\%$, but are still $\sim 10\%$ larger than AVA results computed by projection.

IV. DISCUSSION

Tab. I includes cases with normal AVA (i.e. between $2.5 - 4.5\,\mathrm{cm}^2$) and normal PD (i.e. $< 5\,\mathrm{mmHg}$), but also cases that would be classified[2] as mild (AVA $> 1.5\,\mathrm{cm}^2$; PD $< 20\,\mathrm{mmHg}$) or moderate stenosis ($1.0\,\mathrm{cm}^2 <$ AVA $< 1.5\,\mathrm{cm}^2$; $20\,\mathrm{mmHg} <$ PD < 40 mmHg). Case 9, 10 and 12 come close to cases with severe AV stenosis (i.e. AVA $< 1.0\,\mathrm{cm}^2$; PD $> 40\,\mathrm{mmHg}$). In addition, cases with normal ejection fraction (EF) (i.e. $55 - 75\%$) and reduced EF are included for varying degree of AV stenosis. This comparison of the values in Tab. I with thresholds used in the echocardiographic assessment of AV stenosis shows that the values are realistic and that the 22 analyzed cases cover different conditions. It should be kept in mind, however, that the thresholds for classification refer to the echocardiographic assessment of AV stenosis, while the values in Tab. I have been derived from CT images. Differences in spatial and temporal resolution, imaging artifacts, but also the way actual measurements are done can lead to deviations.

Fig. 11a and b illustrate the origin of the difference between projected and planimetric AVA. Because of the crown-like structure of the AV, the planimetric and the projected AVA correspond only in the central region. The regions at the rim of the triangularly-shaped AVA (arrows in Fig. 11b) are open in the plane where the planimetric AVA is measured, but the valve leaflets downstream of this plane (arrow in Fig. 11a) obstruct the blood flow. When shifting the plane downstream, the AV leaflets do not build a contiguous opening anymore and the blood flow is only partially constrained by the valve leaflets. According to Ref. 1, the geometric AVA is formed by the free edges of the AV leaflets and caution is needed to ensure that the minimum orifice area is identified with planimetry rather than a larger apparent area proximal to the cusp tips. Our projection-based AVA values come close to this definition of the geometric AVA and the planimetric AVA values overestimate the orifice area therefore.

The planimetric AVA that constrains the blood flow when passing the AV, was larger

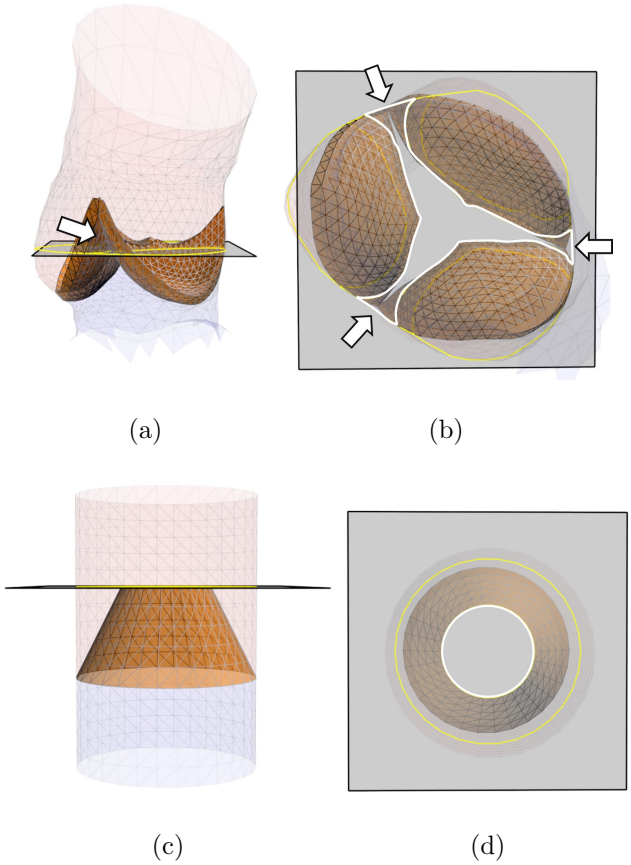

FIG. 11. Illustration of projected and planimetric AVA for an AV model derived from a CT image (a,b) and a simplified AV model used in theoretical fluid mechanics studies[5] (c,d). The plane (a,c) corresponds to the cross-section with minimum orifice area. The white line (b,d) indicates the planimetric AVA in views along the AV axis from the LVOT towards the AA. The arrows (a,b) indicate areas causing differences between projected and planimetric AVA.

than the EOA (Fig. 10a). This observation is in agreement with results from fluid dynamics theory for simplified AV models (Fig. 11c and d) showing that the EOA is smaller than or equal to the geometric orifice area that constrains blood flow through the AV[5]. In addition, the valve leaflets downstream of the planimetric measurement plane obstruct the blood flow and likely contribute to a reduced EOA compared to the planimetric AVA.

The projection-based AVA was clearly smaller than the EOA for EOA values $< 2.0\text{cm}^2$ (Fig. 10b). This observation seems to contradict the theoretical result that the EOA is always smaller than or equal to the geometric orifice area. As mentioned before, the AV leaflets do not build a contiguous opening downstream of the planimetric measurement plane anymore and the blood flow is only partially constrained. The simplified AV model of Fig. 11c and

d (planimetric AVA is equal to the projected AVA for this AV model) does not describe this property of the AV anatomy. EOA values larger than projection-based AVA values are, therefore, not in contradiction to fluid dynamics theory.

We explain the differences between our findings and previous theoretical investigations[5] and in vitro experiments[4], therefore, by the more detailed AV anatomies used in this study. Even when taking all the limitations of the segmentation and simulation approach into consideration (see Sec. III C), the AV models derived from CT images represent the AV anatomy much better than the AV models used in theoretical studies (see Fig. 11). In addition, the CT images have a higher spatial resolution than the echocardiography images used in Ref. 4 and enable in combination with the advanced segmentation algorithm a much better representations of the 3D crown-like structure of the AV to be generated.

V. CONCLUSIONS

An approach for the automatic segmentation of the AV and heart anatomy over the cardiac cycle in cardiac CT angiography images based on the SCDM framework[11,12] was presented. In particular, a structured AV model was constructed, parameterized to describe the AV in different opening states and complemented with information such as connections between the leaflet layers to enable accurate AV segmentation. After integration into a more comprehensive heart model, geometric models of LV, LVOT, AV and the AA were derived from cardiac CT angiography images over the entire heart cycle for 22 patients with non-calcified and (partially) severely calcified tricuspid AVs.

The geometric models were to used compute the geometric AVA by planimetry and by a projection-based approach. The projection-based AVA is closely related to the definition that the minimal orifice area is formed by the free edges of the AV leaflets, and planimetric AVA values were always larger than the projection-based values. The geometric models were also used to perform steady-state CFD simulations and to compare the AVA values with EOA estimates computed via the Bernoulli equation from the CFD-based PD results. AVA and EOA values show a high correlation ($R^2 = 0.97$). An important observation was that the AVA formed by the free edges of the AV leaflets was smaller than the EOA for EOA values $< 2.0\text{cm}^2$. This observation is in contradiction to previous studies that reported that the EOA is always smaller or equal to the geometric AVA. The contradiction is explained

by the more detailed AV models used in this study that better represent the crown-like 3D structure of the AV.

The results contribute to a better understanding of clinically used quantities for characterizing AV stenosis in general, and to understanding the influence of the 3D structure of the AV on the relation between AVA, EOA and PD in particular. The simulation pipeline could also provide a starting point for a CT-based method to assess the PD across the AV complementary to established approaches such as echocardiography or invasive pressure measurements. The high correlation between AVA and EOA might allow for an accurate assessment of the PD on the basis of geometric quantities without performing blood flow simulations.

ACKNOWLEDGMENTS

A. Lungu is funded by the UK Engineering & Physical Sciences Research Council. This work was supported by NRW, Germany and the European Union (Med in.NRW 005-GW01-235C). The research leading to these results has also received funding from the European Unions Horizon 2020 research and innovation programme under grant agreement No 689617. This publication reflects only the views of the authors, and the Union is not liable for any use that may be made of the information contained herein.

DISCLOSURE OF CONFLICTS OF INTEREST

J. Peters, I. Waechter-Stehle, F.M. Weber and J. Weese are employees of Philips.

REFERENCES

[1]N. Saikrishnan, G. Kumar, F. J. Sawaya, S. Lerakis, and A. P. Yoganathan, "Accurate assessment of aortic stenosis: A review of diagnostic modalities and hemodynamics," Circulation **129**, 244–253 (2014).

[2]H. Baumgartner, J. Hung, J. Bermejo, J. Chambers, A. Evangelista, B. Griffin, B. Iung, C. Otto, P. Pellikka, and M. Quiñones, "Echocardiographic assessment of valve stenosis: EAE/ASE recommendations for clinical practice," Eur J Echocardiogr **10**, 1–25 (2009).

[3]O. Klass, M. J. Walker, M. E. Olszewski, J. Bahner, S. Feuerlein, M. H. Hoffmann, and A. Lang, "Quantification of aortic valve area at 256-slice computed tomography: Comparison with transesophageal echocardiography and cardiac catheterization in subjects with high-grade aortic valve stenosis prior to percutaneous valve replacement," Euro J Radiol **80**, 151 – 157 (2011).

[4]D. Gilon, E. Cape, M. Handschumacher, J.-K. Song, J. Solheim, M. VanAuker, M. King, and R. Levine, "Effect of three-dimensional valve shape on the hemodynamics of aortic stenosis: Three-dimensional echocardiographic stereolithography and patient studies," J Am Coll Cardiol **40**, 1479 – 1486 (2002).

[5]D. Garcia and L. Kadem, "What do you mean by aortic valve area: Geometric orifice area, effective orifice area, or gorlin area?" J Heart Valve Dis **15**, 601 – 608 (2006).

[6]R. Ionasec, I. Voigt, B. Georgescu, Y. Wang, H. Houle, F. Vega-Higuera, N. Navab, and D. Comaniciu, "Patient-specific modeling and quantification of the aortic and mitral valves from 4-d cardiac CT and TEE," IEEE Trans Med Imaging **29**, 1636–1651 (2010).

[7]I. Waechter, R. Kneser, G. Korosoglou, J. Peters, N. Bakker, R. Boomen, and J. Weese, "Patient specific models for planning and guidance of minimally invasive aortic valve implantation," in *Medical Image Computing and Computer-Assisted Intervention - MICCAI 2010*, Lecture Notes in Computer Science, Vol. 6361 (2010) pp. 526–533.

[8]S. Grbic, R. Ionasec, D. Vitanovski, I. Voigt, Y. Wang, B. Georgescu, N. Navab, and D. Comaniciu, "Complete valvular heart apparatus model from 4d cardiac CT," Med Image Anal **16**, 1003 – 1014 (2012).

[9]F. M. Weber, T. Stehle, I. Waechter-Stehle, M. Götz, J. Peters, S. Mollus, J. Balzer, M. Kelm, and J. Weese, "Analysis of mitral valve motion in 4d transesophageal echocardiography for transcatheter aortic valve implantation," in *Statistical Atlases and Computational Models of the Heart - STACOM 2014*, Lecture Notes in Computer Science, Vol. 8896 (2015) pp. 168–176.

[10]A. M. Pouch, S. Tian, M. Takebe, J. Yuan, R. Gorman Jr., A. T. Cheung, H. Wang, B. M. Jackson, J. H. Gorman III, R. C. Gorman, and P. A. Yushkevich, "Medially constrained deformable modeling for segmentation of branching medial structures: Application to aortic valve segmentation and morphometry," Med Image Anal **26**, 217–231 (2015).

[11]O. Ecabert, J. Peters, H. Schramm, C. Lorenz, J. von Berg, M. J. Walker, M. Vembar, M. E. Olszewski, K. Subramanyan, G. Lavi, and J. Weese, "Automatic model-based

segmentation of the heart in CT images," IEEE Trans Med Imaging **27**, 1189–1201 (2008).

[12]O. Ecabert, J. Peters, M. Walker, T. Ivanc, C. Lorenz, J. v. Berg, J. Lessick, M. Vembar, and J. Weese, "Segmentation of the heart and great vessels in CT images using a model-based adaptation engine," Med Image Anal **15**, 863–876 (2011).

[13]G. Korosoglou, G. Gitsioudis, I. Waechter-Stehle, J. Weese, U. Krumsdorf, E. Chorianopoulos, W. Hosch, H.-U. Kauczor, H. A. Katus, and R. Bekeredjian, "Objective quantification of aortic valvular structures by cardiac computed tomography angiography in patients considered for transcatheter aortic valve implantation," Cathet Cardiovasc Intervent **81**, 148–159 (2013).

[14]J. D. Hart, G. Peters, P. Schreurs, and F. Baaijens, "A three-dimensional computational analysis of fluid-structure interaction in the aortic valve," J Biomech **36**, 103 – 112 (2003).

[15]C. Carmody, G. Burriesci, I. Howard, and E. Patterson, "An approach to the simulation of fluid-structure interaction in the aortic valve," J Biomech **39**, 158 – 169 (2006).

[16]S. C. Shadden, M. Astorino, and J.-F. Gerbeau, "Computational analysis of an aortic valve jet with lagrangian coherent structures," Chaos **20**, 017512 (2010).

[17]V. Mihalef, R. I. Ionasec, P. Sharma, B. Georgescu, I. Voigt, M. Suehling, and D. Comaniciu, "Patient-specific modelling of whole heart anatomy, dynamics and haemodynamics from four-dimensional cardiac CT images," Interface Focus **1**, 286–296 (2011).

[18]E. Votta, T. B. Le, M. Stevanella, L. Fusini, E. G. Caiani, A. Redaelli, and F. Sotiropoulos, "Toward patient-specific simulations of cardiac valves: State-of-the-art and future directions," J Biomech **46**, 217–228 (2013).

[19]J. Peters, A. Lungu, F. M. Weber, I. Waechter-Stehle, D. Rodney Hose, and J. Weese, "Comparison of CFD-based and bernoulli-based pressure drop estimates across the aortic valve enabled by shape-constrained deformable segmentation of cardiac CT images," in *Biomedical Simulation - ISBMS 2014*, Lecture Notes in Computer Science, Vol. 8789 (2014) pp. 211–219.

[20]N. Piazza, P. de Jaegere, C. Schultz, A. E. Becker, P. W. Serruys, and R. H. Anderson, "Anatomy of the aortic valvar complex and its implications for transcatheter implantation of the aortic valve," Circ Cardiovasc Interv **1**, 74–81 (2008).

[21]R. Haj-Ali, G. Marom, S. B. Zekry, M. Rosenfeld, and E. Raanani, "A general three-dimensional parametric geometry of the native aortic valve and root for biomechanical modeling," J Biomech **45**, 2392 – 2397 (2012).

[22]J. Peters, O. Ecabert, C. Meyer, R. Kneser, and J. Weese, "Optimizing boundary detection via simulated search with applications to multi-modal heart segmentation," Med Image Anal **14**, 70–84 (2010).

[23]J. Peters, J. Lessick, R. Kneser, I. Waechter, M. Vembar, O. Ecabert, and J. Weese, "Accurate segmentation of the left ventricle in computed tomography images for local wall thickness assessment," in *Medical Image Computing and Computer-Assisted Intervention - MICCAI 2010*, Lecture Notes in Computer Science, Vol. 6361 (2010) pp. 400–408.

[24]S. F. Stewart, E. G. Paterson, G. W. Burgreen, P. Hariharan, M. Giarra, V. Reddy, S. W. Day, K. B. Manning, S. Deutsch, M. R. Berman, M. R. Myers, and R. A. Malinauskas, "Assessment of CFD performance in simulations of an idealized medical device: Results of FDA's first computational interlaboratory study," Cardiovasc Eng Technol **3**, 139–160 (2012).

[25]A. Brown, *Patient-specific local and systemic haemodynamics in the presence of a left ventricular assist device.*, Ph.D. thesis, The University of Sheffield (2012).

[26]F. Tan, A. Borghi, R. Mohiaddin, N. Wood, S. Thom, and X. Xu, "Analysis of flow patterns in a patient-specific thoracic aortic aneurysm model," Comput Struct **87**, 680 – 690 (2009).

[27]P. Roache, "Perspective - a method for uniform reporting of grid refinement studies," J Fluids Eng **116**, 405–413 (1994).

Case	EF	ϕ sel.	$dV/d\phi$	$d\phi/dt$	Q	A_{LVOT}	A_{AA}	A_{AVproj}	A_{AVplan}	Δp_{CFD}	A_{EOA}
	%	%	cm^3	BPM	ml/s	cm^2	cm^2	cm^2	cm^2	mmHg	cm^2
1	64.8	20	3.91	61	397	3.81	5.22	2.69	2.80	5.1	2.58
2	51.6	20	2.71	63	285	3.86	5.34	2.74	2.85	2.2	2.72
3	47.4	30	3.62	66	397	4.01	5.62	2.80	2.90	3.7	2.87
4	44.4	20	3.94	51	334	4.92	7.90	1.76	2.02	8.1	2.11
5	22.9	20	1.57	82	214	5.42	8.91	1.62	1.91	4.2	1.94
6	55.4	20	3.38	73	411	4.40	8.00	3.92	4.06	1.5	3.67
7	28.7	30	1.60	98	261	3.84	6.11	1.13	1.33	13.1	1.35
8	18.2	20	1.05	87	152	3.05	4.69	2.30	2.36	1.2	2.06
9	23.8	20	1.76	74	217	5.38	6.76	0.88	1.21	16.3	1.05
10	67.0	30	3.35	57	319	4.13	7.96	1.02	1.37	25.8	1.20
11	75.1	20	1.81	78	235	2.92	5.38	1.42	1.65	7.5	1.48
12	34.2	20	2.46	58	238	5.10	8.75	0.79	1.02	27.3	0.89
13	68.9	30	2.41	74	297	3.44	6.38	1.23	1.48	14.5	1.41
14	27.2	20	1.83	97	295	4.54	7.15	1.43	1.72	13.9	1.49
15	73.9	20	2.81	80	374	3.57	7.14	1.31	1.58	22.3	1.44
16	45.0	30	2.51	67	280	4.18	6.63	2.32	2.67	4.4	2.25
17	48.4	30	2.80	66	308	4.36	6.48	3.22	3.32	2.8	2.80
18	54.2	20	3.31	66	365	4.27	6.79	3.34	3.46	2.7	3.07
19	33.9	30	4.08	56	381	5.10	9.57	4.35	4.46	1.7	3.85
20	64.1	00	2.56	63	269	4.45	8.45	2.98	3.12	1.5	3.12
21	58.4	30	3.03	66	333	3.53	5.23	1.28	1.46	20.0	1.37
22	62.7	10	2.06	58	199	2.76	4.76	2.44	2.51	1.5	2.09

TABLE I. Measurements, geometric AVA results computed by projection (A_{AVproj}) and by planimetry (A_{AVplan}), CFD-based PD estimates Δp_{CFD} and CFD-based EOA values derived from the CT images of the 22 patient cases .

Case	Δp_{CFD} mmHg	Δp_{lam} mmHg	$\Delta p_{\mathrm{trans}}$ mmHg	A_{EOA} mm	A_{lam} mm	A_{trans} mm
12	27.3	28.9	28.4	0.89	0.87	0.88
15	22.3	24.5	23.3	1.44	1.39	1.42

TABLE II. PD estimates for different CFD simulations (laminar flow model instead of a turbulence model; transient flow simulation instead of a steady-state simulation) and corresponding EOA estimates.